Università Politecnica delle Marche

Facoltà di Ingegneria

Dipartimento di Ingegneria dell'Informazione

Corso di Laurea in Ingegneria Informatica e dell'Automazione



Tesi di Laurea

Validazione numerica di un modello matematico geometricamente esatto di un braccio robotico flessibile

Numerical validation of a geometrically-exact mathematical model of a flexible robotic arm

Relatore

Prof. Simone Fiori

Candidato

Francisco Mateo Cassetta

Anno Accademico 2025-2026

Alla mia dolce metà,
stella polare e inseparabile compagna di avventure,
che ha saputo tenermi la mano in ogni momento di incertezza
credendo nei miei sogni ancor prima che lo facessi io.
Al nostro amore, che è la mia sicurezza più grande,
e a tutte le pagine del nostro futuro che non
vediamo l'ora di scrivere,
insieme.

A mi querida familia.
Gracias por apoyarme a su manera,
dándome,
incluso entre incomprensiones,
el impulso para llegar hasta aquí.
Aunque no seamos perfectos,
seguiremos siempre unidos .

E infine, a me.
A tutte le volte in cui ho dubitato delle mie capacità.
Per non essermi mai arreso, scoprendo lungo il percorso
una forza e una determinazione che non sapevo di avere.
Grazie per non aver mollato.

"まだだ!"
Asta, Black Clover

Sommario

Questa tesi analizza il comportamento dinamico di strutture robotiche flessibili mediante l'implementazione di una teoria geometrica esaminata in [4]. L'obiettivo principale consiste nel validare questo modello variazionale, il quale descrive lo stato del robot attraverso un asse baricentrico e gli orientamenti istantanei delle sezioni all'interno del gruppo $\mathbb{SO}(3)$. Al fine di garantire un elevato grado di realismo fisico, la simulazione si concentra su una struttura robotica soft realizzata in elastomero siliconico, caratterizzata dalle sue specifiche proprietà iperelastiche e dissipative. Inoltre, ciascuna sezione trasversale del robot è modellata come un cilindro pieno, non cavo, con una sezione circolare uniforme lungo l'intera lunghezza.

Lo studio è stato sviluppato in ambiente MATLAB® per risolvere le equazioni di moto non lineari accoppiate, tenendo conto delle interazioni elastiche, gravitazionali e magnetiche. Una parte significativa del lavoro è dedicata alla giustificazione metodologica dei parametri di simulazione e degli operatori matematici scelti per garantire la consistenza fisica, in particolare per quanto riguarda la mappatura delle densità di tensione e di quantità di moto.

Il modello viene valutato sotto varie condizioni al contorno per dimostrarne l'adattabilità a differenti vincoli fisici. I risultati confermano che la formulazione cattura accuratamente le ampie deformazioni non lineari e le risposte magnetiche. Ciò dimostra l'efficacia del modello per la progettazione e la simulazione di sistemi robotici soft in ambienti complessi.

Abstract

This thesis investigates the dynamic behavior of flexible robotic structures by implementing a geometric theory surveyed in [4]. The primary objective is to validate this variational formulation, which describes the robot's state through a line of centroids and instantaneous section orientations within the $\mathbb{SO}(3)$ group. To ensure a high degree of physical realism, the simulation focuses on a soft robotic structure fabricated from silicone elastomer, characterized by its specific hyperelastic and dissipative properties. Furthermore,each cross section of the robot is modeled as a solid, non-hollow cylinder with a uniform circular cross-section throughout its length.

The study leverages a MATLAB®-based environment to solve the coupled non-linear equations of motion, accounting for elastic, gravitational, and magnetic interactions. A significant portion of the work is dedicated to the methodological justification behind the simulation parameters and the mathematical operators chosen to ensure physical consistency, particularly regarding the mapping of stress and momentum densities.

The model is evaluated under various boundary conditions to demonstrate its adaptability to different physical constraints. The results confirm that the formulation accurately captures large non-linear deformations and magnetic responses. This demonstrates the model's effectiveness for the design and simulation of soft robotic systems in complex environments.

Evolution and applications of soft robotics

Over the last few decades, the field of robotics has witnessed a significant paradigm shift, transitioning from traditional rigid-body robots to flexible and "soft" robotic systems. Unlike conventional robots, which rely on rigid discrete joints and actuators that limit their deployment in delicate or complex environments, flexible robots are designed to provide high mechanical compliance and theoretically infinite degrees of freedom [1]. This technological evolution draws heavy inspiration from nature, mimicking the dexterity and adaptability of organisms lacking a rigid skeleton, such as octopus tentacles, earthworms, or elephant trunks [1]. The utilization of hyperelastic materials, such as silicone elastomers, combined with continuous architectures, has enabled the development of robots capable of continuous deformation and safe interaction with both humans and unstructured environments [10].

In the literature, flexible robots are typically classified into various categories based on their structure, scale, and actuation mechanisms. A prominent category is represented by *continuum robots*, which feature an elongated, slender, and multi-segmented structure capable of executing complex three-dimensional movements [3]. This category includes tendon-driven robots, steerable catheters, and concentric tube robots, all of which offer exceptional maneuverability [5]. Another highly relevant category is *wearable soft robots*, which are designed to adapt to the complex morphology of the human body. These systems utilize soft materials to ensure smooth, safe, and ergonomic physical human-robot interaction, often in direct contact with the skin [10].

The applications of these technologies are vast and span across highly critical sectors. In the medical field, continuum and soft robots are revolutionizing minimally invasive surgery. Thanks to their ability to navigate deep and tortuous anatomical pathways while minimizing their spatial footprint, they are increasingly employed in delicate procedures such as neurosurgery, micro-vascular ophthalmic surgery, and cardiac interventions, where precision and the minimization of patient trauma are fundamental requirements [3, 5]. In the fields of rehabilitation, biomechanics, and assistive care, wearable robots function as soft exoskeletons or haptic interfaces, assisting individuals with motor impairments in their daily activities or serving as tools for functional hand recovery [1, 10].

Beyond clinical and biomedical domains, the versatility of these systems makes them ideal tools for industrial applications, space exploration, and deep-sea research [6]. *Soft grippers*, for instance, are widely used in the manufacturing industry for the manipulation of fragile or heterogeneously shaped objects. They can spontaneously conform to the geometry of the target object without causing damage [1]. Furthermore, in the exploration of hostile or unstructured environments, flexible robots can navigate narrow spaces and overcome obstacles with great naturalness, operating effectively in scenarios where traditional rigid-body rovers would easily get stuck [6].

It is within this innovative research context that the present work is situated.

Contents

1 Introduction and theoretical framework **12**
1.1 Kinematic configuration and reference frames 12
1.2 Mechanical descriptors 12
1.3 Equations of motion and equilibrium conditions 14
1.4 Energy and momenta: Values and rate of changes 15
1.5 Constitutive characterization and parameter identification 17

2 Numerical validation **19**
2.1 General numerical treatment of derivatives 19
2.2 Geometric integration and rotational kinematics 20
2.3 Numerical solution of static equations: Accelerated gradient descent 20

3 Results of numerical simulations **22**
3.1 Clamped ends, no magnetic field 23
3.2 One clamped end, one free end 29
3.2.1 Without the presence of a magnetic field 29
3.2.2 Presence of a magnetic field 34

4 Conclusion **40**

References **41**

List of Figures

1 Evolution of the Hamiltonian $H(t)$ during the double clamp simulation. 25
2 Evolution of the robot's length over time during the double clamp simulation. 26
3 Time evolution of the translational momentum components during the double clamp simulation. 27
4 Final state of the double clamp simulation: The dynamic solution (blue) perfectly overlaps with the static reference (red). The full animated evolution is available at *this link*. 28
5 Evolution of the Hamiltonian $H(t)$ during the single clamp field free simulation. 30
6 Evolution of the robot's length over time during the single clamp field free simulation. . . 31
7 Time evolution of the translational momentum components during single clamp field free simulation. 32
8 Final state of the single-clamp field free simulation: the dynamic configuration (blue) perfectly recovers the static reference (red). The full animated evolution is available at this link. 33
9 Evolution of the Hamiltonian $H(t)$ during the single clamp simulation under the presence of the magentic field. 36
10 Temporal evolution of the length during the activation of the magnetic field in the single-clamp simulation. 37
11 Time evolution of the translational momentum during the single clamp simulation under the influence of the magnetic field. 38
12 Final state of the magnetic simulation: the dynamic configuration (blue) perfectly recovers the static reference (red). The full animated evolution is available at *this link*. 39

List of Tables

1 Model variables and units (expressed in the International Unit System, where m = meter, kg = kilogram, s = second, Wb = Weber, rad = radians, — = unitless). 15
2 Summary of experimental configurations and boundary conditions. 23
3 Physical and numerical parameters extracted from the MATLAB simulation setup (double clamp simulation). 29
4 Physical and numerical parameters from MATLAB simulation setup (single clamp simulation). 34
5 Physical and numerical parameters from MATLAB simulation setup (single clamp magnetic field simulation). 39

1 Introduction and theoretical framework

This section establishes the mathematical and physical foundations required to describe the behavior of a magnetic soft robot. The theoretical framework is built upon a geometrically exact formulation, which allows for a high-fidelity representation of large deformations and multi-physics interactions. The discussion begins in Section 1.1, where we define the kinematic configuration by introducing the reference frames and the Lie group representation $\mathbb{SO}(3)$ necessary to track the robot's centerline and its local orientations. Building upon this geometric base, Section 1.2 introduces fundamental mechanical descriptors such as material strain, torsion, and generalized momenta. Crucially, this part of the work also defines the mathematical operators—including the skew-symmetric projection σ—and the mapping between standard and non-standard (dual) tensors, providing the essential tools for a consistent formulation of the dynamics.

These descriptors lead directly to the core of the model in Section 1.3, where the equations of motion and the steady-state equilibrium conditions are detailed, accounting for the combined effects of gravity and external magnetic induction fields. To ensure the physical consistency and numerical stability of the model, Section 1.4 provides a comprehensive energy analysis, focusing on the system's Hamiltonian and its rate of change over time. The framework is then completed in Section 1.5 with the constitutive characterization of the material, which explains how the physical properties of silicone and the geometric cross-section are translated into the numerical stiffness and damping parameters used in the simulations.

1.1 Kinematic configuration and reference frames

The equations of motion of a flexible robot are established with respect to two sets of reference frames: An inertial reference frame, and a moving reference frame fixed to each cross-section. The deformed state of a robot can be described by two functions, namely $\phi : [0,\ L] \times [0,\ T] \to \mathbb{R}^3$, which represents the configuration of the line of centroids of the robot, and $R : [0,\ L] \times [0,\ T] \to \mathbb{SO}(3)$, which represents the instantaneous orientation of each section. The constant $L > 0$ can be interpreted as the length of the centerline in an undeformed configuration, while the constant $T > 0$ denotes the time-span of an observation. In the above definitions, the symbol $\mathbb{SO}(3)$ denotes the Lie group of three-dimensional rotations (or *special orthogonal group*).

1.2 Mechanical descriptors

The mathematical framework relies on the operator $\sigma : \mathbb{R}^{3\times3} \to \mathfrak{so}(3)$, defined as $\sigma(X) := \frac{1}{2}(X - X^\top)$, which projects a square matrix into the space of skew-symmetric matrices.
To characterize the physical state of the robot's body, we introduce the material strain $\epsilon : [0,\ L]\times[0,\ T] \to \mathbb{R}^3$ and the material torsion $\Gamma : [0,\ L] \times [0,\ T] \to \mathfrak{so}(3)$. These descriptors are defined as:

$$\epsilon := R^\top \partial_x \phi, \quad \Gamma := \sigma(R^\top \partial_x R). \tag{1}$$

The velocity of each section is described by the angular velocity matrix $\Omega \in \mathfrak{so}(3)$, which is defined as:

$$\Omega := \sigma(R^\top \partial_t R). \tag{2}$$

The symbol $\mathfrak{so}(3)$ denotes the Lie algebra associated to the special orthogonal group (i.e., the set of 3×3 skew-symmetric matrices), while symbols $\partial_x R$ and $\partial_t R$ denote naïve derivatives (Jacobians).

The internal forces are captured by the stress density per unit of length along the body of the robot, defined as:

$$n := C(\epsilon - \mathrm{e_x}). \tag{3}$$

In these relations, the symbol $\mathrm{e_x} \in \mathbb{R}^3$ denotes the unit vector associated with the undeformed centerline, which is assumed to be straight; instead C denotes a 3×3 diagonal stiffness matrix related to axial/shear deformations.

We define the internal momentum density along the body of the robot as:

$$M := \sigma(D\Gamma). \tag{4}$$

This variable accounts for bending and torsional momenta, where D denotes a 3×3 diagonal stiffness matrix related to bending/torsion deformations

Furthermore, the dynamic state of each cross-section is characterized by the translational momentum density per unit of length, $q \in \mathbb{R}^3$, and the angular momentum density per unit of length, $\Pi \in \mathrm{SO}(3)$, defined as:

$$q := \varrho_0 \, \partial_t \phi, \quad \Pi := \sigma(J\Omega). \tag{5}$$

In these relations, ϱ_0 represents the material density per unit of length, while J denotes the material surface rotational inertia tensor. Care should be taken that the rotational stiffness matrix D and the inertia tensor J are *non-standard* (or *dual*) versions. The following result derives the relationship between a standard tensor and its dual.

Lemma 1. *A symmetric,* 3×3*, tensor* T *and its non-standard version* $\bar{T}$ *are related by* $\bar{T} = \frac{1}{2}\,\mathrm{tr}(T) I_3 - T$*, where* $\mathrm{tr}(\star)$ *denotes matrix trace and* I_3 *denotes the* 3×3 *identity matrix.*

Proof. Let us take any vector $x = [x_1 \; x_2 \; x_3]^\top \in \mathbb{R}^3$ and its associated skew-symmetric matrix

$$X := \begin{bmatrix} 0 & -x_3 & x_2 \\ x_3 & 0 & -x_1 \\ -x_2 & x_1 & 0 \end{bmatrix}. \tag{6}$$

The duality of the tensors T and $\bar{T}$ is revealed by the equivalence of the quadratic forms $x^\top T x$ and $\mathrm{tr}(X^\top \bar{T} X)$, which may be verified by direct substitution. □

A closely related result concerns the solution of equations of the type $S = \sigma(\Delta X)$, in the unknown $X \in \mathfrak{so}(3)$, where $S \in \mathfrak{so}(3)$ is given, Δ denotes a positive-definite, diagonal, 3×3 given matrix.

Lemma 2. *Let* $\Delta := \mathrm{diag}(\delta_x, \delta_y, \delta_z)$ *denote a positive-definite, diagonal matrix, and let* $X \in \mathfrak{so}(3)$ *denote a skew-symmetric matrix. The following identity holds:* $\sigma(\bar{\Delta} X) = QXQ$*, where* $\bar{\Delta}$ *denotes the non-standard version of* Δ*, and*

$$Q := \mathrm{diag}\left(\sqrt{\frac{\delta_y \delta_z}{2\delta_x}}, \sqrt{\frac{\delta_x \delta_z}{2\delta_y}}, \sqrt{\frac{\delta_x \delta_y}{2\delta_z}}\right). \tag{7}$$

Proof. The identity may be verified by direct substitution. □

1.3 Equations of motion and equilibrium conditions

The equations of motion of a flexible robot, expressed in terms of generalized variables, read as follows:

$$\boxed{\begin{cases} \epsilon = R^\top \partial_x \phi, \ \Gamma = \sigma(R^\top \partial_x R), \\ q = \varrho_0 \, \partial_t \phi, \ \Pi = \sigma(J\Omega), \ n = C(\epsilon - \mathrm{e_x}), \ M = \sigma(D\Gamma), \\ \partial_t q = \partial_x (R\, n) - g \varrho_0 \, \mathrm{e_z} + \varrho_0 \, \partial_\phi^\top b \, R \, m + f, \\ \partial_t \Pi + [\Omega, \Pi] = \partial_x M + [\Gamma, M] + \sigma(n \epsilon^\top) - \varrho_0 \, \sigma(m \, b^\top R) + \Theta, \\ f = -\mu q, \ \Theta = -\psi \Omega. \end{cases}} \tag{8}$$

where $[X, Y] := XY - YX$ denotes matrix commutator. In the above relations, the constant $g > 0$ denotes the local gravitational acceleration, $\mathrm{e_z} \in \mathbb{R}^3$ denotes the vertical unit vector – directed upward – so that the product $\mathrm{e_z}^\top \phi$ denotes the altitude of each centroid. The vector field $b : \mathbb{R}^3 \times [0, \ T] \to \mathbb{R}^3$ denotes a (possibly time-varying) magnetic induction field acting on the robot's body, and the vector field $m : [0, \ L] \to \mathbb{R}^3$ denotes the specific magnetic dipole moment per unit of mass of each section of the robot. In the above equations, the vector field $f \in \mathbb{R}^3$ represents a further external force field, which is used to take into account, e.g., friction. Likewise, the vector field $\Theta \in \mathfrak{so}(3)$ represents a further external torque field.

It is worth recalling that *the equation of translation of the line of centroids is expressed in the inertial reference frame, while the equation of rotational dynamics about each section is expressed in the body-fixed reference frame attached to that section.* The principal variables used in the model are summarized in Table 1.

Table 1: Model variables and units (expressed in the International Unit System, where m = meter, kg = kilogram, s = second, Wb = Weber, rad = radians, — = unitless).

Quantity	**Description**	**Unit**
ϕ	Position of the centerline in the global frame	m
R	Rotation matrix representing the local orientation	—
ϵ	Translational strain vector	—
Γ	Rotational strain (curvature and torsion) matrix	1/m
q	Translational momentum density vector per unit of length	kg/s
Π	Angular momentum density matrix per unit of length	kg·m·rad/s
n	Internal force vector (normal and shear forces)	kg·m/s^2
M	Internal moment matrix (bending and twisting moments)	kg·m^2/s^2
Ω	Angular velocity matrix	rad/s
ρ_0	Mass density per unit of length	kg/m
b	External magnetic field vector	Wb/m^2
m	Magnetic moment vector per unit mass (of the x-section of the robot)	m^2/(s^2·Wb)
C, D	Stiffness matrices (D is a non-standard matrix)	kg·m/s^2 , kg·m^3/s^2
μ, ψ	Damping coefficients	1/s, kg·m/(rad·s)
J	Non-standard rotational inertia tensor per unit length	kg·m
f	External distributed forces per unit of length	kg/s^2
Θ	External distributed moments per unit of length	kg·m/s^2

Further details on the above-recalled mathematical model can be found in the source paper [4].

Based on the equations of motion (8), the equilibrium configuration defined by the centerline $\phi_\star(x)$ and orientation $R_\star(x)$ is governed by the following system:

$$\boxed{\begin{cases} \epsilon_\star = R_\star^\top \mathrm{d}_x \phi_\star, \ \Gamma_\star = \sigma(R_\star^\top \mathrm{d}_x R_\star), \\ n_\star = C(\epsilon_\star - \mathrm{e_x}), \ M_\star = \sigma(D\Gamma_\star), \\ \mathrm{d}_x(R_\star\, n_\star) - g\varrho_0\, \mathrm{e_z} + \varrho_0\, (\partial_{\phi_\star} b)^\top\, R_\star\, m = 0, \\ \mathrm{d}_x M_\star + [\Gamma_\star, M_\star] + \sigma(n_\star \epsilon_\star^\top) - \varrho_0\, \sigma(m\, b^\top R_\star) = 0. \end{cases}} \tag{9}$$

where d_x denotes the total derivative $\mathrm{d}/\mathrm{d}x$, and the magnetic induction field b is assumed to be time-invariant. The solution $(\phi_\star, R_\star)$ predicts the asymptotic configuration of the robot's body corresponding to zero kinetic energy. The external forces and torques, other than those due to friction, have been ignored for simplicity.

1.4 Energy and momenta: Values and rate of changes

To properly characterize the physical behavior of the magnetic soft robot, it is necessary to define the energy components that govern its dynamics. The energetic state of the robot is defined by the sum of kinetic, elastic, and potential energy densities.

Specifically, the kinetic energy density $K(x,t)$ accounts for both translational and rotational inertia of the robot, as defined below:

$$K(x,t) = \tfrac{1}{2}\|\partial_t \phi(x,t)\|^2 \rho_0(x) + \tfrac{1}{2}\mathrm{tr}(\Omega^\top(x,t) J(x) \Omega(x,t)). \tag{10}$$

The internal elastic response is captured by the strain energy density $E(x,t)$, which penalizes deviations from the reference configuration in terms of both shearing/stretching and bending/twisting:

$$E(x,t) := \tfrac{1}{2}(\epsilon(x,t) - \mathrm{e_x})^\top C(x)(\epsilon(x,t) - \mathrm{e_x}) + \tfrac{1}{2}\operatorname{tr}(\Gamma^\top(x,t)D(x)\Gamma(x,t)). \tag{11}$$

The potential energy density $U(x,t)$ per unit of length includes the external contributions from both the gravitational field and the magnetic interaction:

$$U(x,t) := g\mathrm{e_z}^\top \phi(x,t)\rho_0(x) - b^\top(\phi(x,t),t)R(x,t)m(x)\rho_0(x). \tag{12}$$

Finally, the Hamiltonian $H(t)$, representing the total energy of the system, is obtained by integrating these energy densities over the entire length L of the robot:

$$H(t) := \int_0^L K(x,t)\,\mathrm{d}x + \int_0^L E(x,t)\,\mathrm{d}x + \int_0^L U(x,t)\,\mathrm{d}x. \tag{13}$$

The definition of this function is essential for the subsequent analysis, as the evolution of $H(t)$ provides a fundamental reference to evaluate the physical consistency of the model and the energetic balance of the system during the optimization process.

In particular, during motion, the robot is a non-isolated system that exchanges energy with the surrounding environment. The rate of change of the Hamiltonian, which characterizes the power balance, was derived in [4] as:

$$\begin{aligned} \mathrm{d}_t H = \; & (\partial_t \phi)^\top R\, n\big|_{x=0}^{x=L} + \operatorname{tr}(\Omega^\top M)\big|_{x=0}^{x=L} \\ & - \mu \int_0^L \rho_0 \|\partial_t \phi\|^2\,\mathrm{d}x - \psi \int_0^L \|\Omega\|_{\mathrm{F}}^2\,\mathrm{d}x \\ & - \int_0^L \varrho_0\,(\partial_t b)^\top R\, m\,\mathrm{d}x, \end{aligned} \tag{14}$$

where the symbol $\|\cdot\|_{\mathrm{F}}$ denotes the Frobenius norm. In this relation, the first two terms quantify the energy exchange with the boundary, the third and fourth addenda represent the energy loss due to friction, and the last term accounts for the power exchanged with the magnetic field.

Beyond the energetic analysis, the dynamic behavior is also described by the total translational momentum of the robot, defined as:

$$\bar{q}(t) := \int_0^L q(x,t)\,\mathrm{d}x. \tag{15}$$

During motion, the robot exchanges translational momentum with the environment at a rate given by:

$$\mathrm{d}_t \bar{q} = R\, n\big|_{x=0}^{x=L} - g\,\bar{\rho}\,\mathrm{e_z} + \int_0^L \varrho_0\,(\partial_\phi b)^\top R\, m\,\mathrm{d}x - \mu\bar{q}, \tag{16}$$

where $\bar{\rho}$ denotes the total mass of the robot.

In addition, to monitor the deformation of the body, the instantaneous length of the robotic arm at time t is calculated using the rectification formula applied to its centerline:

$$\bar{L}(t) := \int_0^L \|\partial_x \phi(x,t)\|\mathrm{d}x. \tag{17}$$

This value $\bar{L}(t)$ fluctuates over time, capturing the global effect of the stretching and compression of the robot's sections.

1.5 Constitutive characterization and parameter identification

In the previous section, the internal stress and momentum densities were defined through the 3×3 diagonal stiffness matrices C and D. Following the geometrically exact formulation proposed by Simo and Vu-Quoc [8] and the recent variational developments by Fiori [4], these matrices represent the link between the material's elastic properties and the rod's geometric section.

The mechanical response of the material is governed by three fundamental parameters:

- **Young's modulus (Y)**: Represents the tensile elasticity, or the tendency of an object to deform along an axis when opposing forces are applied along that axis.
- **Poisson's ratio (ν)**: Measures the "Poisson effect," by which a material tends to expand in directions perpendicular to the direction of compression, or contract in directions perpendicular to the direction of stretching.
- **Shear modulus (G)**: Defines the material's response to shear stress (sliding deformation). It is related to Y through the Poisson's ratio by the relation $G := \frac{Y}{2(1+\nu)}$ [9].

We shall assume the body of the robot to be made of cylindrical sections of equal radii. For a circular cross-section of radius r_0 and area $A := \pi r_0^2$, the matrix C, which accounts for shear and stretch stresses, is defined as:

$$C := \mathrm{diag}(YA, GA\kappa, GA\kappa). \tag{18}$$

Although many theoretical formulations, such as the one presented in [8], ignore this fact, the explicit multiplication by the shear factor κ is necessary for physical consistency. In a real 3D robot, the shear stress distribution is not uniform across the section (it is zero at the boundaries and maximum at the neutral axis). Since the 1D theory assumes a constant shear strain across the section, κ acts as a calibration constant that ensures the strain energy in the 1D model matches the actual 3D energy. Without this factor, the numerical model would exhibit an artificial *shear locking* effect or an overestimation of the stiffness. For a solid circular section, we adopt the formulation by Cowper [2]:

$$\kappa := \frac{6(1+\nu)}{7+6\nu} \tag{19}$$

The standard matrix D defines the rotational stiffness, and is constructed as:

$$D = \mathrm{diag}(GJ_\ell,\ YJ_c,\ YJ_c) \tag{20}$$

where the diagonal components are determined by the following geometric properties [9]:

- **Torsional Rigidity (GJ_ℓ)**: Resistance to twisting about the longitudinal axis, with $J_\ell := \frac{\pi r_0^4}{2}$.
- **Flexural Rigidity (YJ_c, YJ_c)**: Resistance to bending moments, with $J_c := \frac{\pi r_0^4}{4}$.

In the formulation for geometrically exact rods proposed by Simo and Vu-Quoc [8], the internal forces include a dissipative component linearly dependent on the strain rate. In this thesis, the internal viscosity of the material is not modeled. In particular, the friction force due to the surrounding fluid is expressed as $f := -\mu\, q$, while the friction torque field is expressed as $\Theta := -\psi\, \Omega$, with μ, $\psi > 0$.

2 Numerical validation

Regarding the numerical implementation, the robot's body is discretized into a series of thin elements, which can be modeled as thin disks. Consequently, the standard inertia-density tensor J is defined as follows:

$$J = \begin{bmatrix} \frac{\rho_0 r_0^2}{2} & 0 & 0 \\ 0 & \frac{\rho_0 r_0^2}{4} & 0 \\ 0 & 0 & \frac{\rho_0 r_0^2}{4} \end{bmatrix} \tag{21}$$

The numerical simulation of the soft robot dynamics is implemented in a MATLAB® environment, discretizing the continuous body of the robot. The core of the computational engine lies in the integration of the coupled non-linear equations of motion (8), ensuring both physical consistency and numerical stability through specific geometric operators.

In this section, we described the numerical strategies and algorithmic frameworks employed to translate the continuous model into a robust simulation environment. The transition from analytical equations to a discrete computational domain begins in Section 2.1, which describes the general numerical treatment of derivatives. Here, we establish the spatial discretization schemes necessary to approximate the robot's state across its length and through time. Building upon this discrete foundation, Section 2.2 addresses the specific challenges of geometric integration and rotational kinematics, focusing on the preservation of the $\mathbb{SO}(3)$ group properties through Lie group theory. Finally, Section 2.3 describes the numerical method which we implemented to find the solution of the static equations, introducing an accelerated gradient descent scheme.

2.1 General numerical treatment of derivatives

In the transition from the continuous mathematical model presented in the literature to a discrete numerical simulation, the treatment of derivatives is a critical step. Since the state of the soft robot is defined only at specific nodes or time steps, analytical derivatives are replaced by finite difference approximations. This approach allows the algorithm to estimate the rate of change of any physical quantity without requiring an explicit analytical function.

For spatial derivatives along the robot's backbone, the implementation employs a multi-scheme finite difference approach to handle the bounded nature of the domain. For all internal points, a *central difference* scheme is used:

$$\frac{\mathrm{d}f(s)}{\mathrm{d}s} \approx \frac{f(s+\Delta s) - f(s-\Delta s)}{2\Delta s}, \tag{22}$$

where $\Delta s > 0$ denotes the chosen spatial separation between two cross-sections. This symmetric approximation provides second-order accuracy, effectively capturing the local gradient by considering the state of the system both ahead and behind the point of interest.

At the boundaries of the structure, where the symmetry of the central scheme cannot be maintained due to the lack of neighboring nodes, one-sided differences are implemented. Specifically, a *forward difference* is applied at the origin ($s = 0$), and a *backward difference* is applied at the termination point ($s = L$):

$$\left.\frac{\mathrm{d}f(s)}{\mathrm{d}s}\right|_{s=0} \approx \frac{f(\Delta s) - f(0)}{\Delta s}, \quad \left.\frac{\mathrm{d}f(s)}{\mathrm{d}s}\right|_{s=L} \approx \frac{f(L) - f(L - \Delta s)}{\Delta s}. \tag{23}$$

These first-order approximations ensure that the boundary conditions are respected without incurring out-of-bounds indexing errors during the execution of the code.

2.2 Geometric integration and rotational kinematics

To ensure that the rotation matrix R remains within the special orthogonal group $\mathbb{SO}(3)$ during the dynamic simulation, we adopt an integration strategy based on Lie group theory. Instead of using standard additive update rules—which would lead to a rapid loss of orthogonality and physical inconsistency—the update of the angular configuration is performed via the exponential map.

Following the mathematical framework established by Murray *et al.* [7] with respect to exponential mapping, for a given body-fixed angular velocity Ω over a time interval Δt, the updating of a section's attitude reads as follows:

$$R(t + \Delta t) = R(t) \exp(\Omega(t)\Delta t). \tag{24}$$

This approach, implemented in the MATLAB environment through the `expm` function, intrinsically preserves the geometric properties of rotation by evolving the state along the manifold rather than in Euclidean space.

2.3 Numerical solution of static equations: Accelerated gradient descent

To determine the equilibrium configuration $(\phi_\star, R_\star)$, the problem is reformulated as an optimization task. Instead of solving the non-linear differential equations directly, we seek to minimize a scalar objective function $Z(\phi, R)$ representing the total residual error of the system. A Gradient Descent (GD) approach is adopted, specifically enhanced through a momentum-based acceleration scheme to improve convergence speed and stability.

In this implementation, the iterative scheme updates the state variables considering the numerical momentum accumulated from previous iterations. Due to the different numerical scales of forces and torques, two distinct momentum vectors are calculated at each step: $\mathbf{v}^{(\phi)}$ for the centerline positions and $\mathbf{v}^{(R)}$ for the local orientations. The state of the system is updated according to the following system:

$$\begin{cases} \mathbf{v}_{k+1}^{(\phi)} = \beta \mathbf{v}_k^{(\phi)} + \alpha_\phi \nabla Z^{(\phi)} \\ \mathbf{v}_{k+1}^{(R)} = \beta \mathbf{v}_k^{(R)} + \alpha_R \nabla Z^{(R)} \\ \phi_{k+1} = \phi_k + \mathbf{v}_{k+1}^{(\phi)} \\ R_{k+1} = R_k \exp(\mathbf{v}_{k+1}^{(R)}) \end{cases} \tag{25}$$

In these expressions, $\nabla Z^{(\phi)}$ and $\nabla Z^{(R)}$ denote the gradients of the objective function with respect to the translational and rotational degrees of freedom, respectively. These gradients correspond to the residuals of the balance equations (9).

The dynamics of the solver are controlled by two main hyperparameters:

- β (Momentum coefficient): This parameter regulates the "memory" of the solver. By retaining a fraction of the previous velocity, it allows the system to maintain direction in flat regions of the energy landscape and dampens unwanted oscillations in narrow valleys.
- α_ϕ, α_R (Learning rates): These coefficients scale the impact of the current gradient on the update. They determine the step size taken in the direction of the steepest descent and are tuned separately to handle the different physical dimensions and stiffness of translational and rotational residues.

A critical distinction is made in the update of the orientation R. While the centerline position ϕ is updated by adding a standard vector, the rotation matrix must be updated using the exponential map to remain within the special orthogonal group $\mathbb{SO}(3)$.

The process continues until the global gradients fall below a predefined tolerance, ensuring that the resulting configuration satisfies the static balance equations with high precision.

3 Results of numerical simulations

To assess the accuracy and robustness of the proposed numerical framework, the model was validated through two distinct experimental scenarios. The first setup (Section 3.1) involves a double-clamp configuration, where both extremities of the robot are rigidly fixed. The second scenario (Section 3.2) transitions toward a magneto-elastic analysis. Within this section, two different experiments are conducted: the first (Section 3.2.1) focuses on the robot's behavior in the absence of a magnetic field, while the second (Section 3.2.2) introduces the magnetic interaction to highlight the resulting differences in dynamics. In both of these cases, the robot is clamped at only one end, while the other is left free to undergo large deflections. This configuration is used to study the interaction between the elastic properties of the rod and an externally applied uniform magnetic field. To model this interaction, it was assumed that only the last section of the robot is composed of Neodymium. This implementation provides the tip with a specific magnetic dipole moment, enabling the structure to experience and react to the external magnetic field.

It is important to note that, while the field-free baseline maintains standard free-end conditions ($n(L,t) = 0$ and $M(L,t) = 0$), the presence of magnetic actuation redefines the physics at the boundary. As the magnetic torque induces genuine deformations and nonzero strains at the tip, forcing the elastic reactions to zero would create a physical contradiction, leading to numerical instabilities. To ensure consistency and correct energy exchange, the concentrated magnetic force f_{mag} and torque Θ_{mag} must be treated as boundary loads, modifying the natural boundary conditions at $x = L$ to:

$$R(L,t)n(L,t) = f_{\text{mag}}, \quad M(L,t) = \Theta_{\text{mag}}. \tag{26}$$

This physically correct treatment allows the internal force and torque at the distal extremity to be computed directly from the constitutive laws, preserving the geometric integrity of the solution during full magnetic exposure.

At the beginning of both simulations, the robot is assumed to be in an undeformed horizontal state. The initial position and orientation for every section $i \in \{1, \ldots, N\}$ are defined as follows:

- **Position** ϕ: The centerline is defined by placing the center of each discrete section at its midpoint along the x-axis, such that $\phi(x, 0) = (i - 0.5)\Delta x \cdot \mathrm{e_x}$.
- **Orientation** R: Every section starts with a local frame aligned to the global canonical basis, meaning $R(x, 0) = I_3$ (the identity matrix).

The simulations process is divided into two main phases based on the implementation:

1. **Static equilibrium recovery**: Starting from the undeformed configuration, the static equilibrium state is computed using an accelerated gradient method (which we discussed in the previous section).

2. **Dynamic relaxation**: Starting from the undeformed configuration, the system is allowed to evolve dynamically. The spatial discretization is governed by the step $\Delta x = L/N$, which represents the distance between adjacent cross-sections in the reference configuration.

Furthermore, to rigorously verify the consistency of the numerical simulations, the solutions were cross-referenced with two fundamental analytical criteria. First, the conservation of the Hamiltonian, defined in (13), was monitored along the length of the rod to ensure that the energy balance was maintained. Finally, the numerical results were directly compared with the differential equilibrium equations (9) to verify that the discretized configuration represents a valid solution. Additionally, for each scenario, the evolution of the total generalized momentum will be presented according to (15), alongside the monitoring of the robot's total length (16) to verify the absence of unphysical stretching or numerical artifacts.

In both simulations, we will assume that the Hamiltonian starts at exactly zero, since at the initial time $t = 0$ the system is defined by $E(x, 0) = 0$, $K(x, 0) = 0$, and $U(x, 0) = 0$.

A summary of the experimental configurations can be found in Table 2.

Configuration	**Physical meaning**	**Boundary conditions**
Double clamp	Fixed position and orientation at both endpoints.	$q(0,t) = q(L,t) = 0$, $\Omega(0,t) = \Omega(L,t) = 0$.
Single clamp (Field-free)	One end clamped and the other left completely free to deform under gravity.	$q(0,t) = 0,\ \Omega(0,t) = 0$, $n(L,t) = 0,\ M(L,t) = 0$.
Single clamp (Magnetic)	One end clamped, with a Neodymium-tipped free end reacting to an external magnetic field and gravity.	$q(0,t) = 0,\ \Omega(0,t) = 0$, $R(L,t)n(L,t) = f_{\text{mag}}$, $M(L,t) = \Theta_{\text{mag}}$.

Table 2: Summary of experimental configurations and boundary conditions.

3.1 Clamped ends, no magnetic field

In this scenario, the model is tested in a purely mechanical configuration to establish a baseline for numerical performance. The robot is rigidly fixed at both extremities (*double clamp* configuration), with the only external force being gravity acting along the negative z-axis.

Based on the equations of motion (8), the dynamics for the current experimental setup are described

by:

$$\begin{cases} \epsilon = R^\top \partial_x \phi,\ \Gamma = \sigma(R^\top \partial_x R), \\ q = \varrho_0\, \partial_t \phi,\ \Pi = \sigma(J\Omega),\ n = C(\epsilon - \mathrm{e_x}),\ M = \sigma(D\Gamma), \\ \partial_t q = \partial_x (R\, n) - g \varrho_0\, \mathrm{e_z} - \mu q, \\ \partial_t \Pi + [\Omega, \Pi] = \partial_x M + [\Gamma, M] + \sigma(n\epsilon^\top) - \psi\Omega, \end{cases} \tag{27}$$

and following the general formulation (9), the equations defining the equilibrium condition for this setup are given by:

$$\begin{cases} \epsilon = R^\top \mathrm{d}_x \phi,\ \Gamma = \sigma(R^\top \mathrm{d}_x R), \\ n = C(\epsilon - \mathrm{e_x}),\ M = \sigma(D\Gamma), \\ \mathrm{d}_x (R\, n) = g \varrho_0\, \mathrm{e_z}, \\ \mathrm{d}_x M + [\Gamma, M] + \sigma(n\epsilon^\top) = 0. \end{cases} \tag{28}$$

These equations can be rewritten in a compact way as

$$\begin{cases} \mathrm{d}_x (R\, C(R^\top \mathrm{d}_x \phi - \mathrm{e_x})) = g \varrho_0\, \mathrm{e_z}, \\ \mathrm{d}_x \sigma(D\sigma(R^\top \mathrm{d}_x R)) + [\sigma(R^\top \mathrm{d}_x R), \sigma(D\sigma(R^\top \mathrm{d}_x R))] + \sigma(C(R^\top \mathrm{d}_x \phi - \mathrm{e_x})(R^\top \mathrm{d}_x \phi)^\top) = 0. \end{cases} \tag{29}$$

The relations above are two coupled differential equations, of the second order, which are equipped with four boundary conditions (two about each variable, see Table 2).

By specializing the general energy balance (14) to the current experimental setup, the energy exchange rate takes the simplified form:

$$\frac{\mathrm{d}H}{\mathrm{d}t} = -\mu \int_0^L \rho_0 \|\partial_t \phi\|^2 \,\mathrm{d}x - \psi \int_0^L \|\Omega\|_{\mathrm{F}}^2 \,\mathrm{d}x, \tag{30}$$

since all other terms are zero. This expression means that the total energy is non-increasing, due to the friction with the surrounding fluid.

As for the dynamic properties, while the general principle is established in (16), the exchange rate of translational momentum for this specific configuration takes the following form:

$$\frac{\mathrm{d}\bar{q}(t)}{\mathrm{d}t} = R(L,t)n(L,t) - R(0,t)n(0,t)\ - g\, \bar{\rho}\, \mathrm{e_z} - \mu\, \bar{q}(t). \tag{31}$$

From this relation, we gather that the equilibrium configuration is one such that $R\, n|_{x=0}^{x=L} = g\, \bar{\rho}\, \mathrm{e_z}$. This relation may be easily interpreted: The two constraints together provide all the suspension force necessary to balance the weight of the robot, namely $R(L,\infty)n(L,\infty) - R(0,\infty)n(0,\infty) = g\, \bar{\rho}\, \mathrm{e_z}$. Interestingly, from this expression alone, it would be impossible to determine the exact force exerted by each constraint, if unknown.

It is important to clarify that, in both of the phases we discussed on the previous sub-section, we iteratively updated the position ϕ and the orientation R only for the internal nodes, specifically for the range $2 : N-1$. By keeping the first ($i = 1$) and the last ($i = N$) nodes excluded from the update loop, the boundary conditions remain fixed, ensuring a rigid clamp at both ends.

The evolution of the Hamiltonian $H(t)$, defined in (13), serves as a fundamental diagnostic tool to monitor the energetic balance of the system. As shown in Figure 1, as the simulation progresses and the robot undergoes gravitational loading and relaxation, the energy curve drops, exhibiting a damped oscillatory behavior. This descent represents the conversion and dissipation of energy until the system reaches a steady-state equilibrium. The stabilization of the curve indicates that the numerical solver has reached a physical balance. It is important to note that minor localized "recoveries" or upward fluctuations in the energy curve may be attributed to inherent numerical artifacts or integration tolerances within the discretized time-stepping scheme.

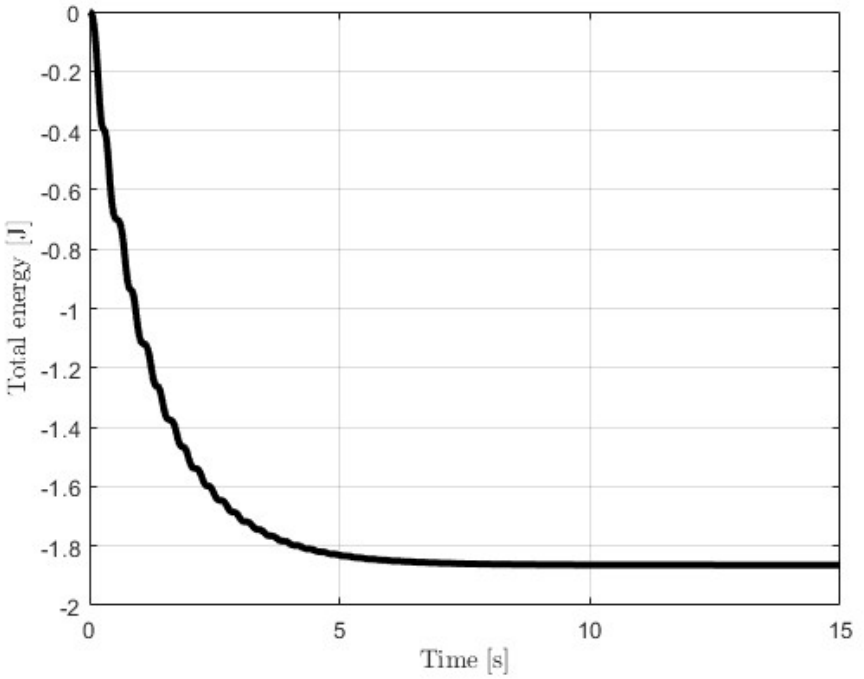


Figure 1: Evolution of the Hamiltonian $H(t)$ during the double clamp simulation.

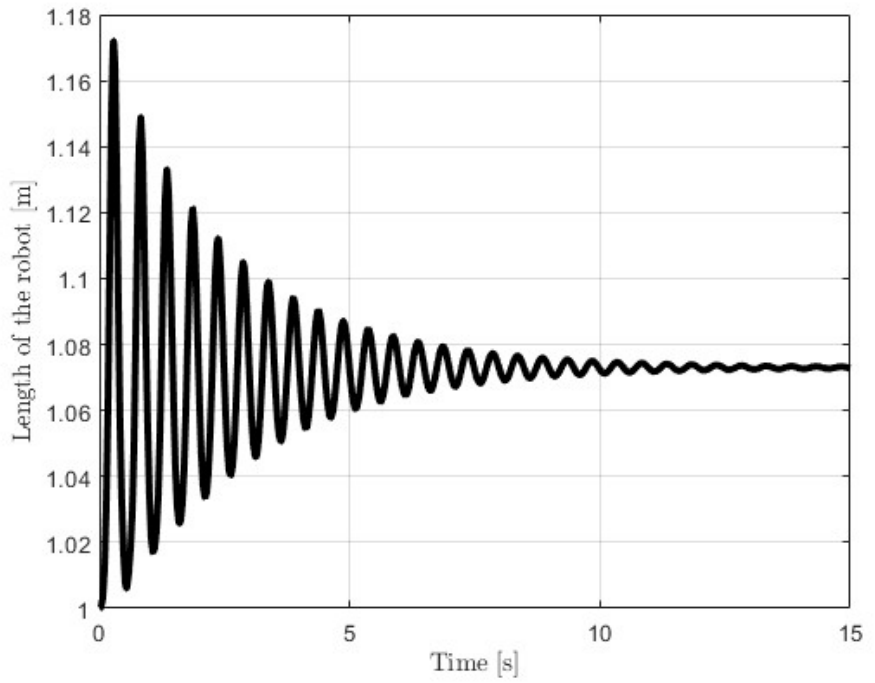


Figure 2: Evolution of the robot's length over time during the double clamp simulation.

The numerical stability of the framework is further evidenced by the evolution of the robot's total length over time, as illustrated in Figure 2. Following an initial transient phase characterized by damped oscillations with the elastic response of the robot and as fluid friction dissipates the system's energy, the robot's length exhibits an asymptotic convergence toward its steady-state equilibrium. This stabilization confirms that the numerical scheme effectively handles the internal constraints, ensuring that the discretized configuration maintains its geometric integrity without introducing unphysical stretching or cumulative errors.

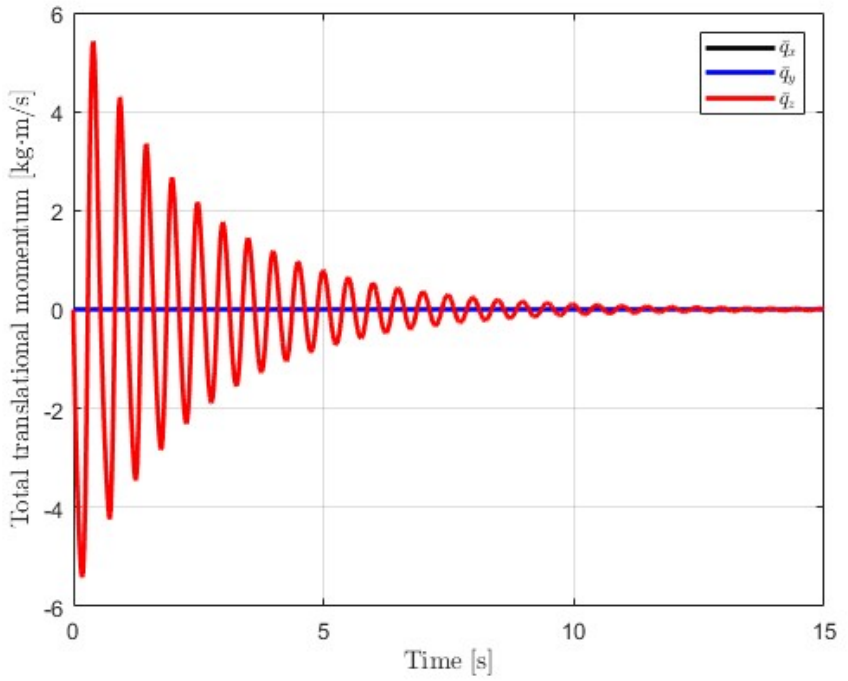


Figure 3: Time evolution of the translational momentum components during the double clamp simulation.

Consistent with the energy dissipation analysis, Figure 3 illustrates the evolution of the total translational momentum. The vertical component $\bar{q}_z$ exhibits the characteristic damped oscillatory behavior as the robot settles into its equilibrium configuration under the influence of gravity. Notably, the components $\bar{q}_x$ and $\bar{q}_y$ remain null throughout the simulation; in particular, $\bar{q}_x$ is not visible as it is perfectly overlapped by $\bar{q}_y$ at the zero baseline. This is due to the symmetry of the double-clamp setup and the absence of longitudinal external forces, which ensures that the dynamics are confined strictly to the vertical plane. The convergence of all components to zero further validates the reach of a stable static equilibrium.

Finally, the alignment between the dynamic evolution and the static reference is further validated by the visual results of the simulation. As demonstrated in the accompanying video, the robot's motion is represented by two overlapping structures: the red ghost-trace, which corresponds to result of the pre-calculated static equilibrium equations, and the blue solid body, which represents the real-time dynamic integration.

Initially, the blue structure oscillates due to the sudden application of gravitational loads, while the red trace remains fixed as a target configuration. Over time, the external damping term dissipates the kinetic energy, leading to a progressive reduction in amplitude.

The physical and numerical parameters used for this simulation are summarized in Table 3.

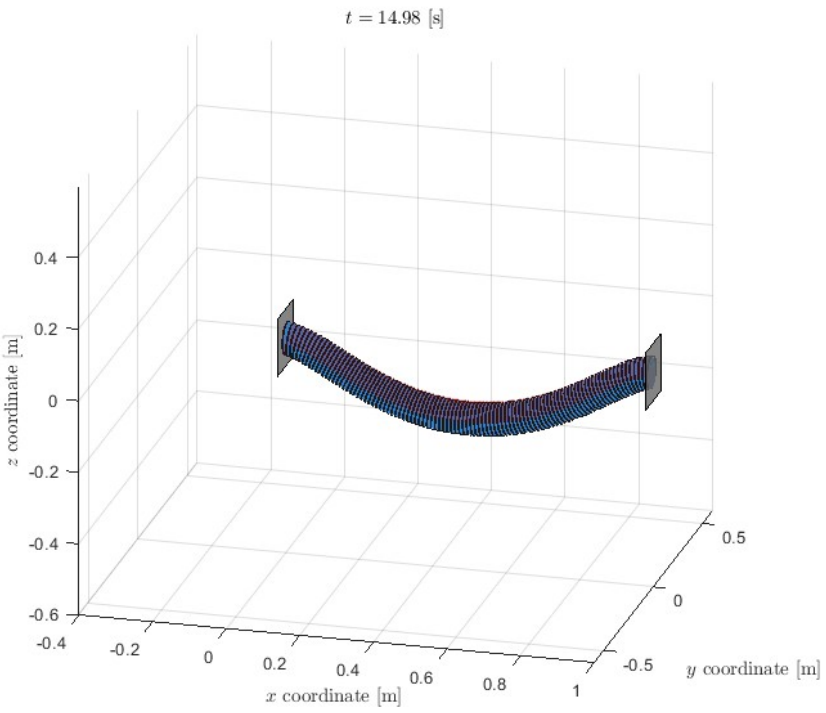


Figure 4: Final state of the double clamp simulation: The dynamic solution (blue) perfectly overlaps with the static reference (red). The full animated evolution is available at *this link*.

Symbol	Description	Value
T	Total simulation time	15 s
Δt	Time-step	5×10^{-4} s
N	Number of sections	100
L	Total rest length	1 m
r_0	Section radius	0.042 m
ρ	Material density	1100 kg/m^3
Y	Young's modulus	0.8×10^5 N/m^2
ν	Poisson's ratio	0.48
g	Gravitational acceleration	9.81 m/s^2
μ	Fluid drag coefficient	0.4 1/s
ψ	Rotational damping	0.2 kg·m/(rad·s)
α_ϕ	Gradient step for position	2×10^{-8}
α_R	Gradient step for orientation	2×10^{-4}
β	Momentum factor	0.96

Table 3: Physical and numerical parameters extracted from the MATLAB simulation setup (double clamp simulation).

3.2 One clamped end, one free end

This chapter explores the behavior of the robot in a single-clamp configuration, where the proximal end is fixed and the distal end ($i = N$) is left free to undergo large deflections and rotations. This specific numerical setup is maintained across both experimental scenarios presented: the field-free baseline and the subsequent simulation under the influence of an external magnetic field. By involving all nodes from $i = 2$ to $i = N$ in the iterative update, the free extremity is allowed to react dynamically to the varying force landscapes. To ensure a rigorous comparison, all physical and structural parameters remain identical across both experiments. The only distinction lies in the second scenario, where the model is augmented with the specific magnetic parameters required to simulate the interaction between the Neodymium-tipped structure and the external field.

3.2.1 Without the presence of a magnetic field

Initially, the system is tested in a field-free environment to validate the purely mechanical response. In this scenario, both the equations of motion (27) and the compact equilibrium form (29) remain valid,

provided boundary conditions are appropriately adjusted for the free distal end (see Table 2). Regarding energetics, the energy exchange follows the dissipative structure of (30), with the Hamiltonian $H(t)$ decreasing monotonically due to friction as the robot settles into its downward gravitational equilibrium. Similarly, the translational momentum exchange maintains the structural form defined in (31), but it is specialized for the free-end condition as follows:

$$\frac{\mathrm{d}\bar{q}(t)}{\mathrm{d}t} = -R(0,t)n(0,t) - g\bar{\rho}\mathrm{e}_\mathrm{z} - \mu\bar{q}(t), \tag{32}$$

where the term relating to the stress at the distal end is null ($n(L,t) = 0$). In this configuration, the entire suspension force required to balance the weight of the robot and the dissipative loads is provided exclusively by the proximal clamp ($x = 0$) and is propagated across its body by elastic interactions.

The influence of this configuration on the energetics of the system is illustrated in Figure 5. In the absence of external magnetic work, the time evolution of the Hamiltonian $H(t)$ exhibits a monotonic decrease, indicating continuous energy dissipation via external damping as the robot settles into its downward gravitational equilibrium.

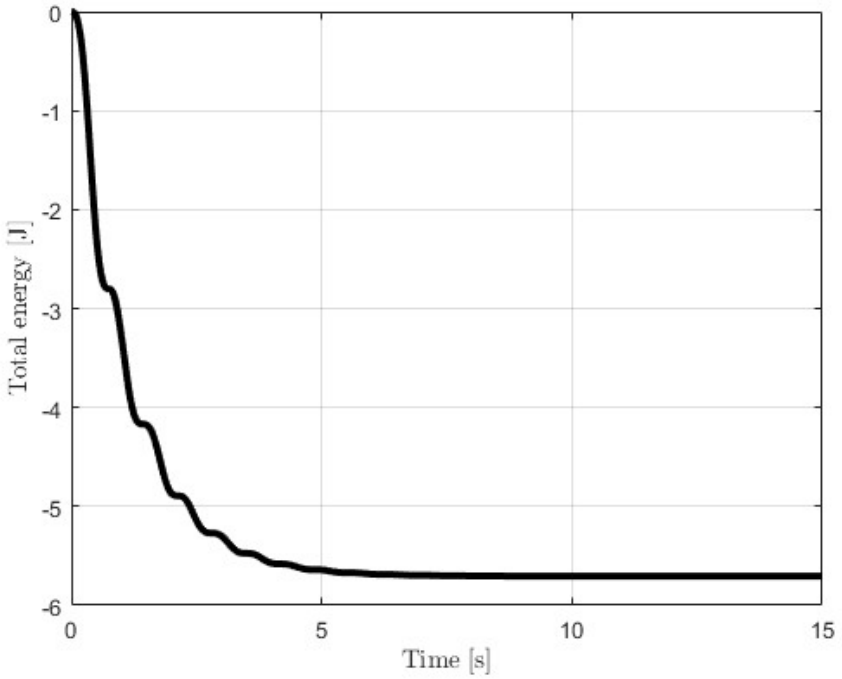


Figure 5: Evolution of the Hamiltonian $H(t)$ during the single clamp field free simulation.

The dynamic response of the system is further characterized by the evolution of the total length of the robot, as shown in Figure 6. Unlike the symmetric oscillations observed in the double-clamp setup, the length variation here appears less uniform and more complex. This behavior is a direct consequence

of the single-clamp configuration: with one end left completely free, the rod undergoes complex coupled longitudinal and lateral swinging motions. These non-linear interactions between different vibration modes cause the irregular oscillation patterns visible in the transient phase. Despite this initial complexity, the damping terms effectively stabilize the system, leading the length to converge asymptotically to its steady-state value as the robot reaches gravitational equilibrium.

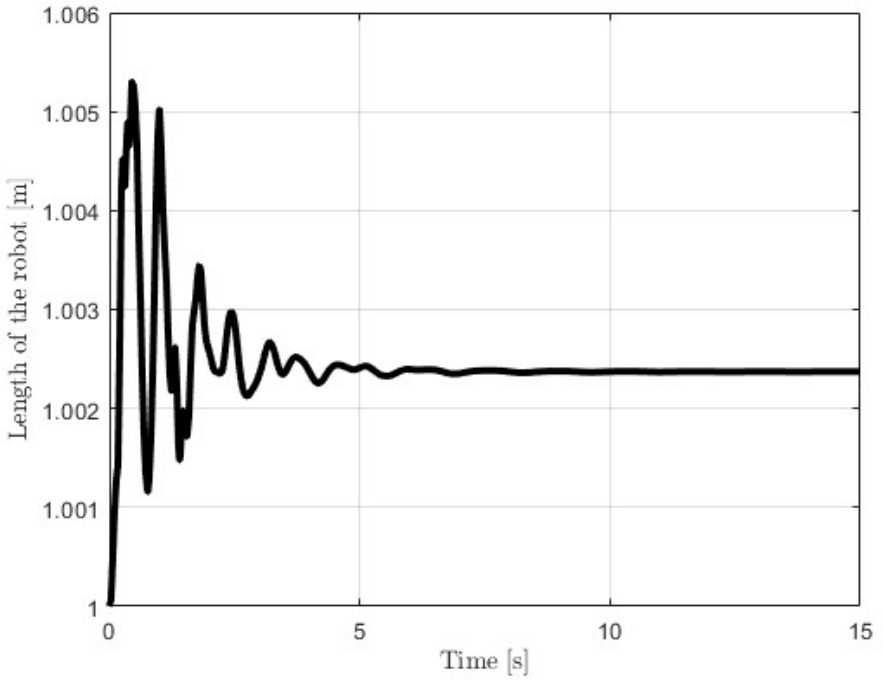


Figure 6: Evolution of the robot's length over time during the single clamp field free simulation.

Furthermore, during the evolution of the total translational momentum, as shown in Figure 7, unlike the previous symmetric double-clamp scenario, the component $\bar{q}_x$ is no longer null during the transient phase. This is because the single-clamp constraint allows the robot to undergo large swings and longitudinal displacements as it falls under gravity. Without a second constraint to restrict the horizontal motion, the rod's center of mass shifts along the x-axis during the oscillation, generating a non-zero momentum component. As the motion is damped, all components, including $\bar{q}_x$, asymptotically converge to zero, marking the achievement of the static equilibrium.

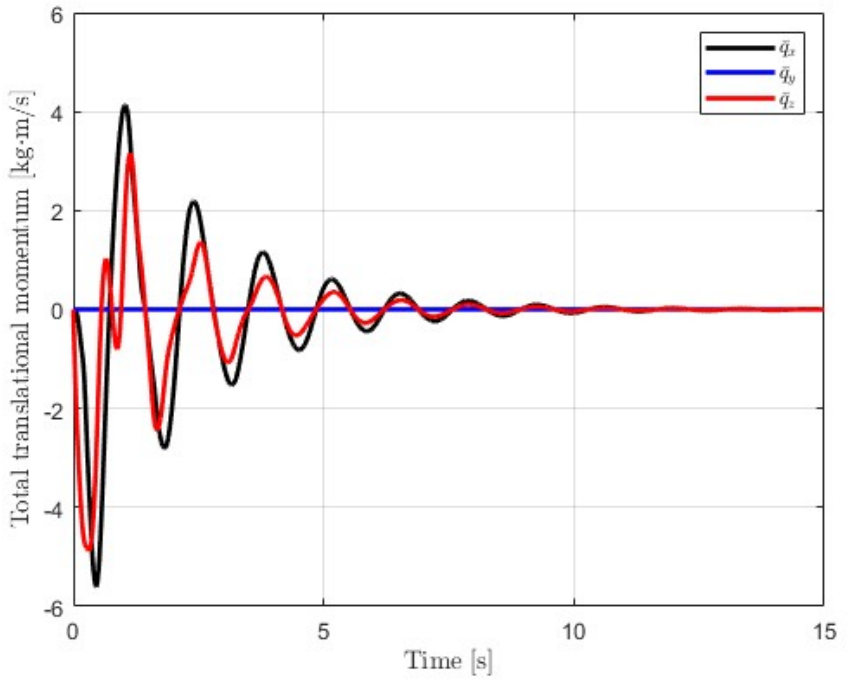


Figure 7: Time evolution of the translational momentum components during single clamp field free simulation.

Finally, the visual consistency between the static reference and the dynamic evolution can be observed in Figure 8, where you can also find the video result. As in the double-clamp simulation, the red structure represents the pre-calculated static equilibrium configuration, while the blue structure shows the real-time dynamic evolution. As expected, the blue robot starts from a predefined initial condition and begins to oscillate due to gravitational acceleration. The external damping coefficient successfully dissipates the kinetic energy, and the dynamic solution smoothly settles onto the red static reference, as seen in the final frame.

The physical and numerical parameters used for this simulation are summarized in Table 4.

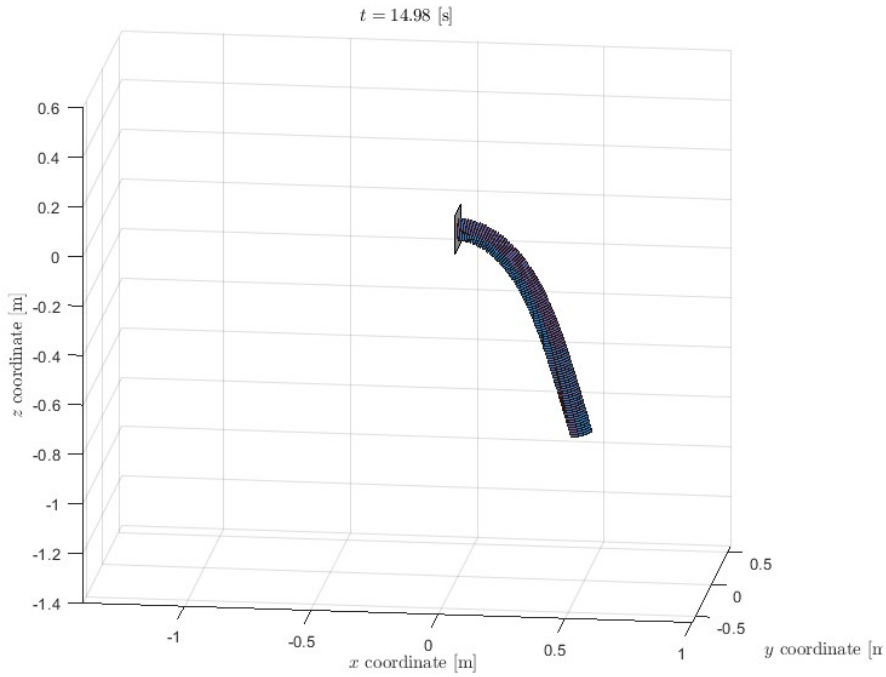


Figure 8: Final state of the single-clamp field free simulation: the dynamic configuration (blue) perfectly recovers the static reference (red). The full animated evolution is available at this link.

Symbol	Description	Value
T	Total simulation time	15.0 s
Δt	Time-step	5×10^{-4} s
τ	Magnetic field time constant	4 s
N	Number of sections	30
L	Total rest length	0.6 m
r_0	Section radius	0.042 m
ρ	Silicone density	800 kg/m^3
Y	Young's modulus	1.2×10^6 N/m^2
ν	Poisson's ratio	0.48
g	Gravitational acceleration	9.81 m/s^2
μ	Fluid drag coefficient	0.5 1/s
ψ	Rotational damping	0.2 kg·m/(rad·s)
α_ϕ	Gradient step for position	4×10^{-8}
α_R	Gradient step for orientation	2×10^{-5}
β	Momentum factor	0.95

Table 4: Physical and numerical parameters from MATLAB simulation setup (single clamp simulation).

3.2.2 Presence of a magnetic field

Having validated the field-free response, the framework is subsequently employed to evaluate the interaction between elastic restoration and magnetic actuation. This setup introduces a localized magnetic moment m at the distal extremity, which is characterized by a Neodymium-based tip. To accurately model this interaction, the magnetic dipole moment is derived from the material's physical properties, specifically, the residual magnetic flux density b_r and the material tip density ρ_m, as follows:

$$m = \frac{b_\mathrm{r}}{4\pi \cdot 10^{-7} \rho_m} \mathrm{e_x}. \tag{33}$$

The entire expression represents the local alignment of the magnet along the robot's axis.

It is worth noting that, while the target magnetic field is time-invariant, it is applied during the dynamic simulation through an exponential smoothing factor:

$$b(t) = \left(1 - e^{-\frac{t}{\tau}}\right) b_\star \tag{34}$$

where τ is a characteristic time constant and $b_\star$ is the time-invariant magnetic field. This gradual activation is necessary to prevent numerical instabilities caused by impulsive magnetic torques, ensuring a smooth transition from the gravitational equilibrium to the final magneto-elastic configuration. In this simulation, the field $b_\star$ is oriented to guide the magnetic tip primarily along the x-axis, with a positive vertical component to induce a slight upward lift in the z-direction.

Referring to the general equations of motion (8), the dynamics for the current magnetic setup are specialized as follows:

$$\begin{cases} \epsilon = R^\top \partial_x \phi, \ \Gamma = \sigma(R^\top \partial_x R), \\ q = \varrho_0, \partial_t \phi, \ \Pi = \sigma(J\Omega), \\ n = C(\epsilon - \mathrm{e_x}), \ M = \sigma(D\Gamma), \\ \partial_t q = \partial_x(Rn) - g\varrho_0, \mathrm{e_z} - \mu q, \\ \partial_t \Pi + [\Omega, \Pi] = \partial_x M + [\Gamma, M] + \sigma(n\epsilon^\top) - \varrho_0 \sigma(m b_\star^\top R) - \psi\Omega. \end{cases} \tag{35}$$

In fact, since the field is uniform in space, the traction force f_{mag} is zero.
Similarly, referring to the general equilibrium equations (9), the static configuration for this setup is given by:

$$\begin{cases} \epsilon = R^\top \partial_x \phi, \ \Gamma = \sigma(R^\top \partial_x R), \\ n = C(\epsilon - \mathrm{e_x}), \ M = \sigma(D\Gamma), \\ \partial_x(Rn) = g\varrho_0 \mathrm{e_z}, \\ \partial_x M + [\Gamma, M] + \sigma(n\epsilon^\top) - \varrho_0 \sigma(m b_\star^\top R) = 0. \end{cases} \tag{36}$$

To incorporate the magnetic contribution into the compact form, we extend the second-order equilibrium system. Similarly to the previous derivation, the compact system is updated as follows:

$$\begin{cases} \mathrm{d}_x(RC(R^\top \mathrm{d}_x \phi - \mathrm{e_x})) = g\varrho_0 \mathrm{e_z}, \\ \mathrm{d}_x \sigma(D\sigma(R^\top \mathrm{d}_x R)) + [\sigma(R^\top \mathrm{d}_x R), \sigma(D\sigma(R^\top \mathrm{d}_x R))] + \\ \sigma(C(R^\top \mathrm{d}_x \phi - \mathrm{e_x})(R^\top \mathrm{d}_x \phi)^\top) - \varrho_0 \sigma(m b_\star^\top R) = 0. \end{cases} \tag{37}$$

By specializing the general energy balance (14) to the magneto-elastic scenario, the energy exchange rate is updated to account for the external magnetic work:

$$\frac{\mathrm{d}H}{\mathrm{d}t} = -\mu \int_0^L \rho_0 ||\partial_t \phi||^2 \ \mathrm{d}x - \psi \int_0^L ||\Omega||_{\mathrm{F}}^2 \ \mathrm{d}x - \int_0^L \varrho_0 (\partial_t b)^\top R m \ \mathrm{d}x. \tag{38}$$

In this expression, the third term accounts for the power injected into the system by the time-varying magnetic field. Crucially, the term $\partial_t b$ is not computed through numerical differentiation; instead, it is defined analytically starting from the activation function $b(t)$. Given its specific form, its time derivative is implemented as:

$$\partial_t b(t) = \frac{1}{\tau} e^{-\frac{t}{\tau}} b_\star. \tag{39}$$

Finally, regarding the dynamic properties, the exchange rate of translational momentum for this magneto-elastic configuration is derived from (16) and takes the following form:

$$\frac{\mathrm{d}\bar{q}(t)}{\mathrm{d}t} = -R(0,t)n(0,t) - g\bar{\rho}\mathrm{e}_\mathrm{z} + \int_0^L \varrho_0(\partial_t b)^\top Rm \ \mathrm{d}x - \mu\bar{q}. \tag{40}$$

In this single-clamp setup, the term $R(L,t)n(L,t)$ is identically zero because the distal end is free from concentrated external loads.

The energy evolution of the system under magnetic actuation is illustrated in Figure 9. At the very beginning of the simulation, a spike in the Hamiltonian can be observed, as the external magnetic field supplies energy to the system.

Following this initial transformation, the curve follows a decreasing trend as the robot is driven into its new shape. The magnetic field acts as a non-conservative source that reconfigures the energy state of the system, guiding it toward a lower potential. The smooth decay toward a constant steady-state value confirms that the damping terms effectively dissipate the kinetic energy, allowing the robot to settle into a stable magneto-elastic equilibrium where the external magnetic torque is perfectly balanced by the internal elastic restoration.

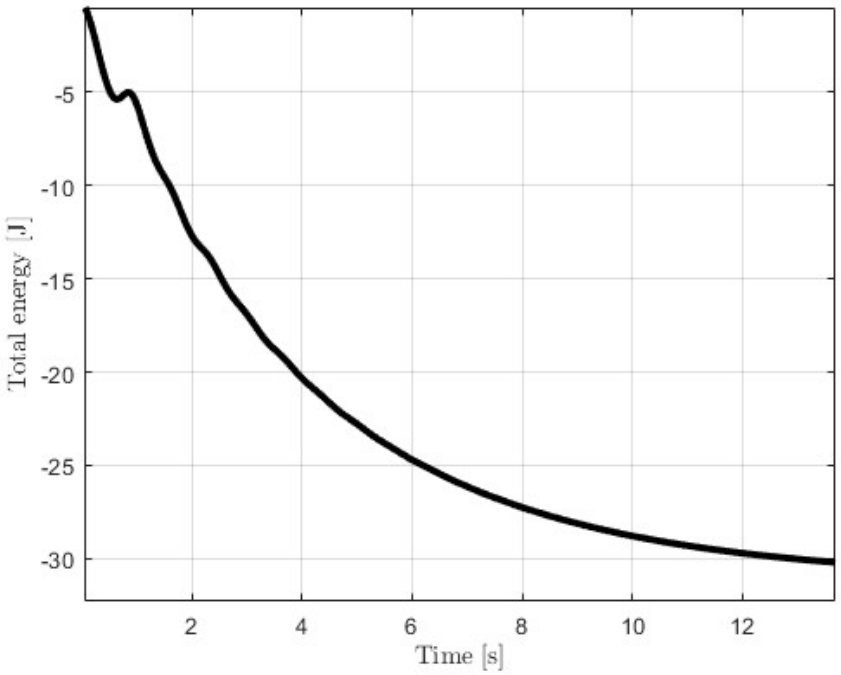


Figure 9: Evolution of the Hamiltonian $H(t)$ during the single clamp simulation under the presence of the magentic field.

The evolution of the robot's total length during the magnetic actuation phase is illustrated in Figure

10.

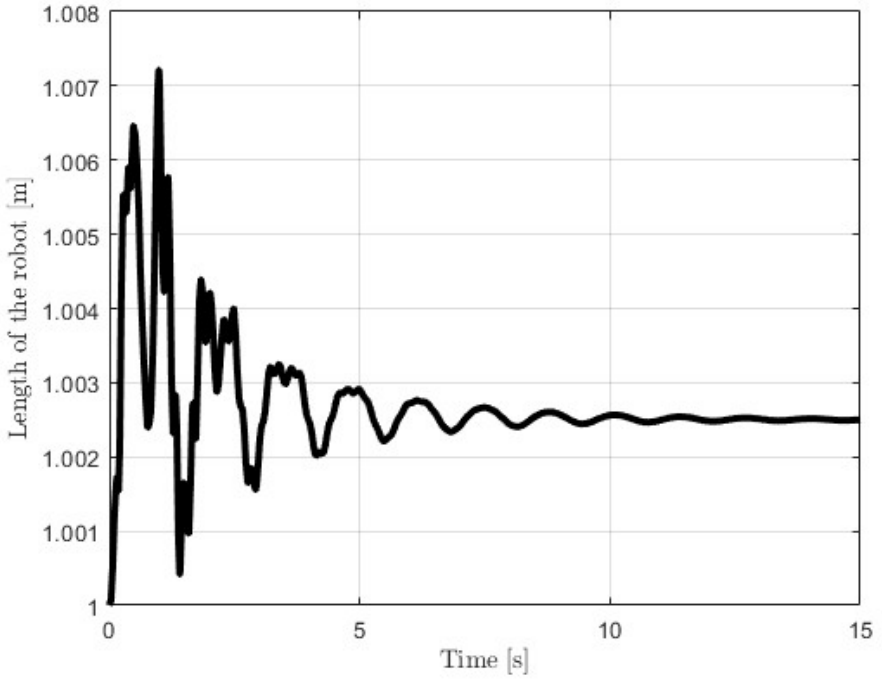


Figure 10: Temporal evolution of the length during the activation of the magnetic field in the single-clamp simulation.

As shown in the figure, the length initially exhibits a series of oscillations. This behavior represents the elastic response of the robot as it reacts to the activation of the magnetic load and the influence of gravity. These fluctuations are a direct consequence of the system's inertia and the dynamic coupling between the internal stresses and the external magnetic torque.

Over time, the amplitude of these oscillations diminishes due to the dissipative effects of the damping terms. The system eventually settles at a constant steady-state value, slightly different from the nominal resting length. This stabilization confirms that the robot has reached a stable magneto-elastic configuration, demonstrating the numerical consistency of the solver throughout the transition from a resting state to a fully actuated equilibrium.

Furthermore, the dynamic response of the system is captured by the evolution of the total translational momentum shown in Figure 11. The plot highlights a sharp initial transience, dominated by oscillations in the vertical direction as the robot reacts to the magnetic activation and gravity. As the damping effects prevail, the momentum smoothly converges to zero, confirming that the robot has reached a stable static equilibrium where the base constraint fully balances all external loads.

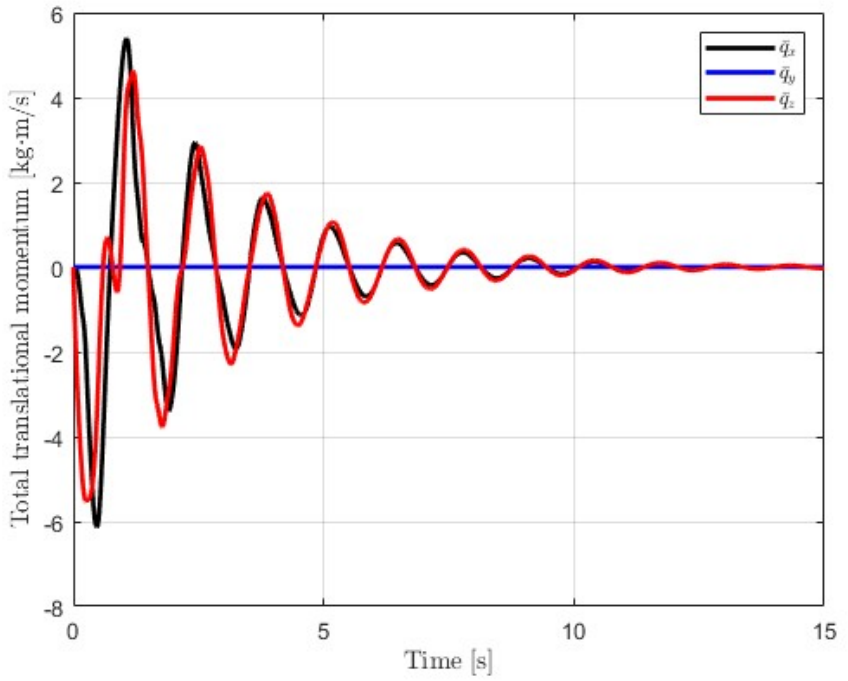


Figure 11: Time evolution of the translational momentum during the single clamp simulation under the influence of the magnetic field.

The numerical consistency of the simulation is further confirmed by the visual analysis of the robot's trajectory. As shown in the final snapshot in Figure 12, the blue dynamic structure effectively tracks the red static reference as the external magnetic field b reaches its nominal value.

Initially, the robot undergoes large-amplitude oscillations due to the combined action of gravity and the exponential ramp-up of the magnetic torque. However, the damping coefficients successfully dissipate the kinetic energy, as previously discussed in the Hamiltonian analysis. By the end of the simulation, the dynamic solution reaches a steady state that perfectly matches the pre-calculated static equilibrium configuration.

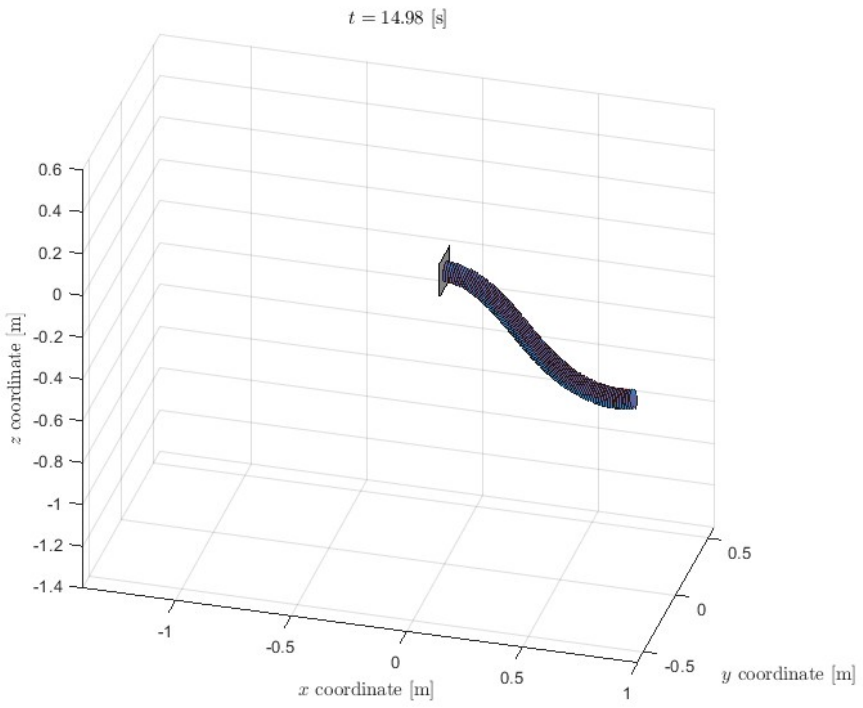


Figure 12: Final state of the magnetic simulation: the dynamic configuration (blue) perfectly recovers the static reference (red). The full animated evolution is available at *this link*.

The physical and numerical parameters used for this simulation are summarized in Table 4 and in Table 5, note that the correct Δt is the one in the last table.

Symbol	**Description**	**Value**
Δt	Time-step	7×10^{-5} s
ρ_m	Neodymium density (tip)	7500 kg/m^3
b_{r}	Residual magnetic flux density	1.2 Wb/m^2
$b_\star$	Nominal external magnetic field vector	$[0.5, 0, 0.25]^\top$ Wb/m^2

Table 5: Physical and numerical parameters from MATLAB simulation setup (single clamp magnetic field simulation).

4 Conclusion

The main purpose of the present project was to conduct a critical review of the theoretical material presented in [4] and to carry out a numerical validation of the geometrically-exact theory discussed therein. A careful re-check of the equations of motion (8) and of the equation of the static equilibrium (9), aided by numerical simulations, revealed that a few terms in the equations were initially reported incorrectly and needed a revision. In addition, in order to proceed with the simulations, plausible values for the many parameters involved in the mathematical model were devised. These values concern mainly the material features of the body of the robot, as well as the features of the specific numerical algorithms employed to carry out the numerical simulations.

In conclusion, this work successfully validated the revised mathematical framework through a series of numerical experiments, ranging from purely elastic relaxation to complex magneto-elastic actuation. The results demonstrate that the proposed model correctly captures the non-linear dynamics and large deflections characteristic of soft robotic structures. The stability of the Hamiltonian and the convergence of the translational momentum confirm the robustness of the integration schemes adopted, even when external non-conservative loads, such as magnetic fields, are introduced.

Looking forward, several promising research directions emerge from this study. Future developments could focus on the design of advanced control strategies to precisely manipulate the robot's trajectory in real-time. Such advancements are crucial for the practical deployment of these soft structures in high-precision fields, most notably in minimally invasive medicine. Developing a reliable control framework would pave the way for the use of magnetic soft robots in surgical applications or targeted drug delivery, where flexibility and delicate interaction with biological tissues are of paramount importance.

References

[1] Z. Chen et al. Data-driven methods applied to soft robot modeling and control: A review. *IEEE Transactions on Automation Science and Engineering*, 2025.

[2] G.R. Cowper. The shear coefficient in Timoshenko's beam theory. *Journal of Applied Mechanics*, 1966.

[3] Y. Feng. A survey of continuum robots deployed in the medical fields. In *2023 4th International Seminar on Artificial Intelligence, Networking and Information Technology (AINIT)*. IEEE, 2023.

[4] S. Fiori. Variational formulation of a fully-three-dimensional non-linear beam dynamics by a Lie-group representation. *AIMS Mathematics*, 10(9):21953–21993, 2025. URL: `https://www.aimspress.com/article/doi/10.3934/math.2025978`.

[5] F. Iqbal et al. Continuum and soft robots in minimally invasive surgery: A systematic review. *IEEE Access*, 2025.

[6] M. Kalekeyeva et al. Continuum robots: Current trends in design, control, and applications. *IEEE Access*, 2025.

[7] R.M. Murray, Z. Li, and S.S. Sastry. *A Mathematical Introduction to Robotic Manipulation*. CRC Press, Boca Raton, FL, 1994.

[8] J. C. Simo and L. Vu-Quoc. A finite strain beam formulation. the three-dimensional dynamic problem. *Computer Methods in Applied Mechanics and Engineering*, 1986.

[9] S.P. Timoshenko and J.N. Goodier. *Theory of Elasticity*. McGraw-Hill, New York, 3rd edition, 1970.

[10] M. Zhu et al. Soft, wearable robotics and haptics: Technologies, trends, and emerging applications. *Proceedings of the IEEE*, 2022.

Ringraziamenti

Vorrei dedicare queste ultime pagine ai ringraziamenti per tutti coloro che mi sono stati vicino e che hanno sempre creduto in me.

Innanzitutto ringrazio di cuore il **professor Simone Fiori** per avermi dato la possibilità di svolgere insieme a **Pietro** l'esperienza fantastica in Cina, alla base di tutto questo lavoro. Per me è stato molto più di un semplice tirocinio; infatti non solo mi ha aiutato a crescere, ma mi ha anche permesso di cimentarmi in questo paese che, apparentemente così diverso dal nostro, allo stesso tempo riesce a trasmettere emozioni molto forti.
It was also very interesting to get to know Professor **Erchuan**, who always took care of us, showing us brand-new places and telling us about Chinese culture. I will always remember the dinners we had all together, chatting about this and that while enjoying unique and unforgettable dishes.

Il ringraziamento più profondo lo dedico a te, mia dolce **Ketty**,
come ho già brevemente introdotto nella dedica, ti sono infinitamente riconoscente per essere sempre stata al mio fianco. Ti ricorderai bene di tutte quelle volte in cui pensavo di non farcela e volevo quindi mollare tutto, ma tu sei sempre stata lì, pronta a tirarmi su di morale e a farmi credere in me stesso un'altra volta. Mi sento davvero fortunato ad avere una donna come te nella mia vita, che ogni giorno mi completa, mi rende felice e mi dà una marcia in più... Ti confesso che senza di te probabilmente non avrei potuto raggiungere questo obiettivo. Quindi grazie, grazie infinite per tutto ciò che fai per me giorno dopo giorno; sappi che ritengo che questo traguardo e questa corona ti appartengano tanto quanto me. Ti prometto che anch'io ti sosterrò sempre, con tutte le mie forze, nel bene e nel male. Mi auguro che questo sia il primo di tanti obiettivi da raggiungere insieme; prossimamente infatti aspetto la tua di laurea: quel giorno voglio essere al tuo fianco come so che tu sarai nel mio. Viviamo questa gara che si chiama vita mano nella mano, superando ogni ostacolo e amandoci sempre di più, giorno dopo giorno.

"Amore è un faro sempre fisso
che sovrasta la tempesta e non vacilla mai,
è la stella polare per le navi erranti."
William Shakespeare, Sonetto 116

Ti amo Ketty, sei la mia stella polare.
Per sempre, il tuo Francisco

Alla mia **sorellina**,
sappiamo bene entrambi che ti bullizzo sempre per essere '06; questo, però, non esclude l'affetto che provo nei tuoi confronti. Sebbene non siamo legati dal sangue, io ti considero a tutti gli effetti tale... Grazie infinitamente per aver sempre fatto il tifo per me e per esserti sempre preoccupata, ti voglio tanto bene! Credi sempre in te stessa, perché con le capacità che hai puoi fare di tutto, ne sono convinto.

A toda mi **familia**: sé todos los sacrificios que hicieron y que hacen para poder ayudarme a estudiar. Aunque a veces peleamos, los quiero muchísimo a todos. Sin ustedes nunca habría podido estar acá y recibir este diploma; esto también es gracias a ustedes. Gracias de corazón por estar todos acá conmigo hoy, me hace muy feliz. Espero que la pasemos genial todos juntos celebrando este momento.
En particular:
A mi **mamá**, por estar siempre a mi lado, creer en mí y quererme mucho;
A mi tía **Karina**, por ayudarme con todas las cosas, a preparar la ropa, la comida, y darme buenos consejos;
A mi tía **Analía**, por buscarme siempre aunque estemos lejos y por interesarse siempre por mí;
A mi nona **María**, que siempre piensa en mí y me hace muchos regalos;
Al nono **Emilio**, que desde que se fue a la Argentina, me llama todos los días y no ve la hora de volver y comer juntos.
Espero que estén orgullosos de mí, gracias de corazón!

A tutti i miei **compagni di università**. Devo dire che è stato davvero bello stare insieme; non dimenticherò mai i momenti passati a lezione, oppure a smattirci per cercare un posto dove studiare (finendo per fare completamente altro). Sono molto felice che alla fine sia riuscito a legare con la maggior parte di voi e, soprattutto, a creare un rapporto che non fosse solo legato allo studio, facendo anche uscite indimenticabili. Auguro a tutti il meglio, sia per il vostro percorso sia per la vita, e spero vivamente che ci ricontreremo nel tempo per aggiornarci e divertirci, ricordandoci di come lo abbiamo fatto in questi anni! Mi mancherete, ragazzi.

A tutti i miei **amici**,
compagni di avventure e di emozioni: scusate per avervi gonfiato la testa con le mie lamentele sull'università... Sappiate che vi voglio bene tutti, dal primo all'ultimo, e sono davvero felice di sapere che sarete presenti in questo momento molto importante per me. Grazie per avermi sempre supportato.

Infine, volevo dedicare qualche parola **a me**. Nel corso di questo percorso mi sono sempre svalutato e spesso mi sono ritrovato insoddisfatto. Voglio dire a quel ragazzo di credere di più in se stesso, perché finalmente, contro ogni sua aspettativa, ce l'ha fatta.
Quindi **a me**, al me che credeva di non farcela e che riteneva di non esser abbastanza.

Non smettere mai di credere ai tuoi sogni, perseguili fino in fondo e vedi che si avvereranno.

Tu puoi. Fighting!

Ancona, 22 ottobre 2026

Un ringraziamento sentito anche al mio fidato compagno, ***Gemini****.*

